Computer Engineering Department at Michigan Technological University for financial support.

REFERENCES

1. V. Derycke, R. Martel, J. Appenzeller, and P. Avouris, Carbon nanotube inter- and intramolecular logic gates, Nano Lett 1 (2001), 453–456.
2. J. Appenzeller, J. Knoch, R. Martel, V. Derycke, S. Wind, and P. Avouris, Carbon nanotube electronics, Nanotechnol IEEE Trans 1 (2002), 184–189.
3. S. Datta, Quantum transport: Atom to transistor, Cambridge University Press, 2005.
4. S. Datta, Nanoscale device modeling: The green's function method, Superlattice Microstruct 28 (2000), 253–278.
5. R. Lake, G. Klimeck, R.C. Bowen, and D. Jovanovic, Single and multiband modeling of quantum electron transport through layered semiconductor devices, J Appl Phys 81 (1997), 7845–7869.
6. R. Venugopal, Z. Ren, S. Datta, M.S. Lundstrom, and D. Jovanovic, Simulating quantum transport in nanoscale transistors: Real versus mode-space approaches, J Appl Phys 92 (2002), 3730–3739.
7. R.H. Bartels and G.W. Stewart, Solution of the matrix equation ax + xb = c [f4], Commun. ACM 15 (1972), 820–826.
8. G. Golub, S. Nash, and C. Van Loan, A hessenberg-schur method for the problem ax + xb = c, automatic control, IEEE Trans 24 (1979), 909–913.
9. R.M. Martin, Electronic structure: Basic theory and practical methods, vol. 1., Cambridge University Press, Cambridge, UK, 2004.
10. P. Pulay, Convergence acceleration of iterative sequences. The case of scf iteration, Chem Phys Lett 73 (1980), 393–398.
11. J.Y. Park, S. Rosenblatt, Y. Yaish, V. Sazonova, H. Üstünel, S. Braig, T.A. Arias, P.W. Brouwer, and P.L. McEuen, Electronphonon scattering in metallic single-walled carbon nanotubes, Nano Lett 71 (2004), 517–520.
12. A. Javey, J. Guo, M. Paulsson, Q. Wang, D. Mann, M. Lundstrom, and H. Dai, High-field quasiballistic transport in short carbon nanotubes, Phys Rev Lett 92 (2004), 106804.
13. G.D. Mahan, Many particle physics, Springer, New York, NY, 2000.
14. G. Pennington and N. Goldsman, Low-field semiclassical carrier transport in semiconducting carbon nanotubes, Phys Rev B 71 (2005), 205318.
15. D.N. Futaba, K. Hata, T. Namai, T. Yamada, K. Mizuno, Y. Hayamizu, M. Yumura, and S. Iijima, 84% catalyst activity of water-assisted growth of single walled carbon nanotube forest characterization by a statistical and macroscopic approach, J Phys Chem B 110 (2006), 8035–8038.
16. S.O. Koswatta, S. Hasan, M.S. Lundstrom, M.P. Anantram, and D.E. Nikonov, Non-equilibrium green's function treatment of phonon scattering in carbon nanotube transistors, IEEE Trans Electron Dev 54 (2007), 2339.
17. R. Saito, G. Dresselhaus, and M.S. Dresselhaus, Physical properties of carbon nanotubes, Imperial College Press, London, UK, 1998.
18. G. Pennington, N. Goldsman, A. Akturk, and A. E. Wickenden, Deformation potential carrier-phonon scattering in semiconducting carbon nanotube transistors, Appl Phys Lett 90 (2007), 062110.
19. F. Leonard, Physics of carbon nanotube devices (micro and nano technologies), William Andrew, 2008.
20. www.nanohub.org using cntphonons tool.
21. S. Piscanec, M. Lazzeri, J. Robertson, A.C. Ferrari, and F. Mauri, Optical phonons in carbon nanotubes: Kohn anomalies, peierls distortions, and dynamic effects, Phys Rev B 75 (2007), 035427.
22. V.N. Popov and P. Lambin, Intraband electron-phonon scattering in single-walled carbon nanotubes, Phys Rev B 74 (2006), 075415.
23. J.W.G. Wildoer, L.C. Venema, A.G. Rinzler, R.E. Smalley, and C. Dekker, Electronic structure of atomically resolved carbon nanotubes, Nature 391 (1998), 59–61.
24. M.P. Anantram and T.R. Govindan, Conductance of carbon nanotubes with disorder: A numerical study, Phys Rev B 58 (1998), 4882–4887.
25. H. Suzuura and T. Ando, Phonons and electron-phonon scattering in carbon nanotubes, Phys Rev B 65 (2002), 235412.
26. A. Bachtold, M.S. Fuhrer, S. Plyasunov, M. Forero, E.H. Anderson, A. Zettl, and P.L. McEuen, Scanned probe microscopy of electronic transport in carbon nanotubes, Phys Rev Lett 84 (2000), 6082–6085.

A THREE-FREQUENCY FEED FOR MILLIMETER WAVE RADIOMETRY

D. J. Hoppe,[1] B. Khayatian,[1] J. B. Sosnowski,[1] P. Bruneau,[1] A. Johnson,[1] S. C. Reising,[2] and S. T. Brown[1]
[1] Jet Propulsion Laboratory, California Institute of Technology, Pasadena, California; Corresponding author: daniel.j.hoppe@jpl.nasa.gov
[2] Department of Electrical and Computer Engineering, Colorado State University, Colorado

Received 14 February 2012

ABSTRACT: *A high-performance millimeter-wave feed, designed for a broad-band radiometry application is presented. The feed provides three separate output ports in the 87–97 GHz, 125–135 GHz, and 161–183 GHz bands. Measured return loss is better than 20 dB in the upper two bands and 15 dB in the lowest band, and good pattern symmetry is obtained throughout all three frequency bands.* © 2012 Wiley Periodicals, Inc. Microwave Opt Technol Lett 54:2483–2487, 2012; View this article online at wileyonlinelibrary.com. DOI 10.1002/mop.27118

Key words: *feed horn; millimeter wave; multifrequency; radiometer*

1. INTRODUCTION

In this article, we describe the electrical and mechanical design as well as the measured performance of a three-frequency millimeter-wave feed horn. The principal objective for development of the feed is to assess the ability of higher-frequency radiometers to meet the needs of the surface water and ocean topography (SWOT) mission recommended by the U.S. National Research Council's Earth Science Decadal Survey, which was accelerated in 2010 and is planned for launch in 2020 [1, 2]. The primary objectives of SWOT are to characterize ocean submesoscale processes on 10-km and larger scales in the global oceans, and to measure the global water storage in inland surface water bodies, including rivers, lakes, reservoirs, and wetlands.

Current satellite ocean altimeters include nadir-viewing, colocated 18–37 GHz multichannel microwave radiometers to measure wet-tropospheric path delay. Because of the area of the surface instantaneous fields of view at these frequencies, the accuracy of wet path retrievals begins to degrade at $\sim$40 km from the coasts. In addition, they do not provide wet path delay estimates over land. A viable approach to meet these needs is the addition of millimeter-wave window channels at 90–170 GHz, with inherently finer spatial resolution for a given antenna size. The addition of these millimeter-wave channels to current Jason-class radiometers is expected to improve retrievals of wet-tropospheric delay in coastal areas and to enhance the potential for over-land retrievals.

For this purpose, wide-band millimeter-wave radiometers have been developed with center frequencies of 90, 130, and 166 GHz to demonstrate new component technology, including PIN-diode switches and noise diodes for internal calibration integrated into the radiometer front-end [3]. A three-frequency broadband millimeter-wave feed is needed to minimize mass and provide a common focal point for all 3 mm-wave bands. In the following sections, we describe the electrical design of the feed, its mechanical aspects, and provide both computed and measured results for return loss and radiation patterns in all three frequency bands.

2. DESCRIPTION

The frequency bands of interest for the SWOT high frequency feed are 87–97 GHz, 125–135 GHz, and 161–183 GHZ. Each band exits the feed in a separate waveguide port, WR10 for the 90 GHz channel, WR8 for the 130 GHz channel, and WR5 for the 170 GHz channel. For this application we require a prime focus feed with an edge taper of $\sim$20 dB at an illumination angle of $\pm 40°$. A single polarization is provided in each band. Preliminary requirements called for a return loss of better than 15 dB across all three bands.

These illumination requirements and relative frequency spacing are similar to that of those required for the scanning multichannel microwave radiometer on Seasat, the (TOPEX)/Poseidon, and the Jason missions, [4]. However in this particular application, the required fractional bandwidth is larger. Thus, the three-frequency feed horn described here shares many features in common with the feed previously developed for the above missions.

A cross sectional view of the HFSS [5] model of the feed is depicted in Figure 1. As shown in the model, to achieve similar E and H plane beam widths over the combined 87–183 GHz band ring loaded slots are used in the corrugated portion of the feed, [6, 7]. Mechanical fabrication of these ring loaded slots for operation up to 183 GHz was particularly challenging, and is discussed further below. The feed operates in a flare-angle limited condition, which gives approximately constant beam width across the entire band and provides a common phase center located near its apex. The half flare angle for the feed is $\sim 30°$. Analysis and optimization of the overall feed design used a combination of finite element (HFSS), and mode-matching (WASPNET) [8], tools.

As shown in Figure 1, the WR5 port is located at the rear of the feed while the copolarized WR8 port enters from the top on the figure. A corrugated low pass filter which provides >30 dB of isolation prevents the 161–183 GHz signals from interacting with the 125–135 GHz port. The location of the filter is chosen to provide an effective short at the waveguide wall in the high frequency band minimizing reflections in that band. After the two high frequency bands are diplexed the waveguide is stepped up to a size large enough to accept the 92 GHz band. This band is injected in the orthogonal polarization using a pair of narrow slots in the common region. Because multiple propagating modes are possible in the higher frequency bands in this region of the feed, a balanced pair of slots is used. A separate combiner is used to merge these two waveguides and provides a single WR10 port for the radiometer.

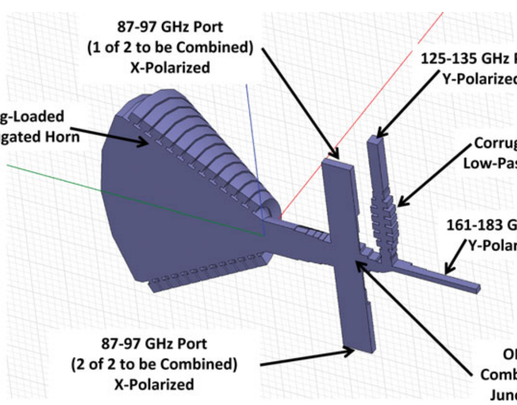

Figure 1 Cross sectional view of the feed. [Color figure can be viewed in the online issue, which is available at wileyonlinelibrary.com]

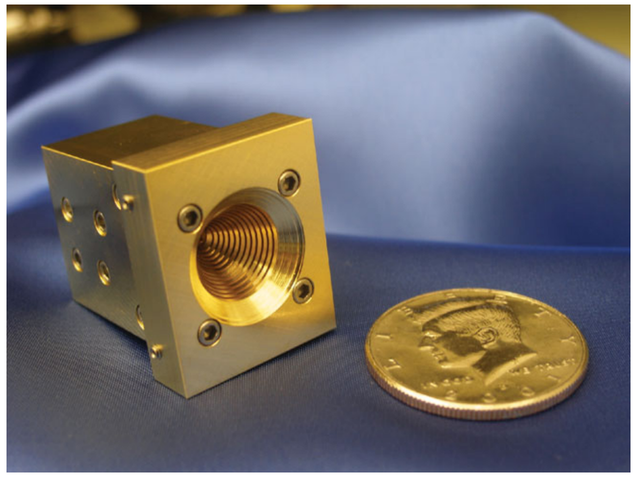

Figure 2 Assembled prototype feed. [Color figure can be viewed in the online issue, which is available at wileyonlinelibrary.com]

Split-block construction is used for the bulk of the feed. The corrugated portion of the feed is built up using a series of rings, which are dropped into the assembled split blocks and encapsulated with an end cap at the aperture of the feed. The two split blocks, end cap, and rings were machined form brass and gold plated. The separate combiner block was fabricated using electroforming.

Operation at frequencies up to 183 GHz demands very high tolerance fabrication techniques. In this instance tolerances of ± 0.0005 inches were specified in the 92 GHz regions of the feed, of ± 0.0003 inches in the 130 GHz regions, and of ± 0.00025 inches in the highest frequency areas. Assembly of the device required fabrication of multiple copies of various components, inspection with a microscope, and rejection of subpar units.

Figure 2 shows the completed feed, with the low frequency combiner absent, along with a quarter for scale. The overall size of the feed, including the combiner block is $\sim$1.00 by 1.25 by 1.50 inches.

3. MEASURED RESULTS

Figures 3–5 summarizes the measured return loss for the feed in each of the three operating bands. As mentioned previously the specification for return loss is better than 15 dB across the operating bandwidth. Figure 3 shows that the feed achieves nearly 20 dB return loss over the 87–97 GHz band. In addition the measured and computed return loss is in excellent agreement. This is indicative of the excellent tolerances held during the manufacturing process.

Figure 4 shows results in the WR8 band where better than 20 dB return loss is achieved from 125 to 136 GHz, with a slight exception around 126 GHz. Once again excellent agreement is between the predicted and measured results is evident.

Return loss in the highest band is shown in Figure 5. A return loss of 20 dB is achieved from approximately 163–187 GHz, rising to 15 dB near 161 and 189 GHz. Excellent agreement between the measured and predicted performance is seen

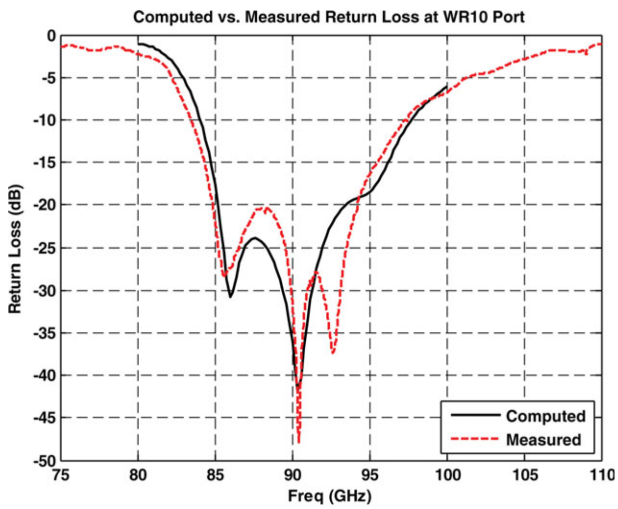

Figure 3 Return loss in the 92 GHz band. [Color figure can be viewed in the online issue, which is available at wileyonlinelibrary.com]

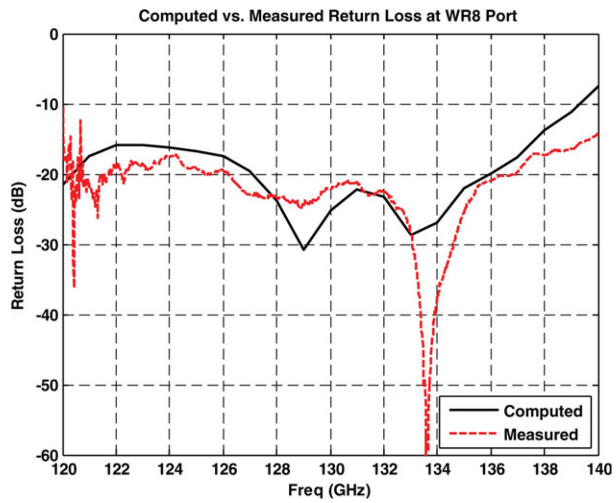

Figure 4 Return loss in the 130 GHz band. [Color figure can be viewed in the online issue, which is available at wileyonlinelibrary.com]

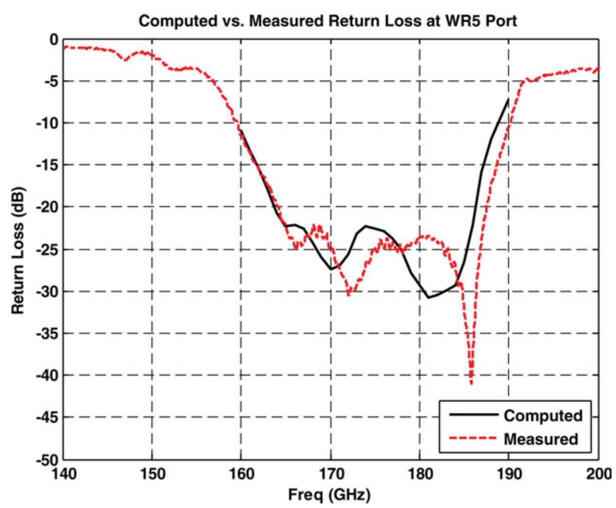

Figure 5 Return loss in the 166 GHz band. [Color figure can be viewed in the online issue, which is available at wileyonlinelibrary.com]

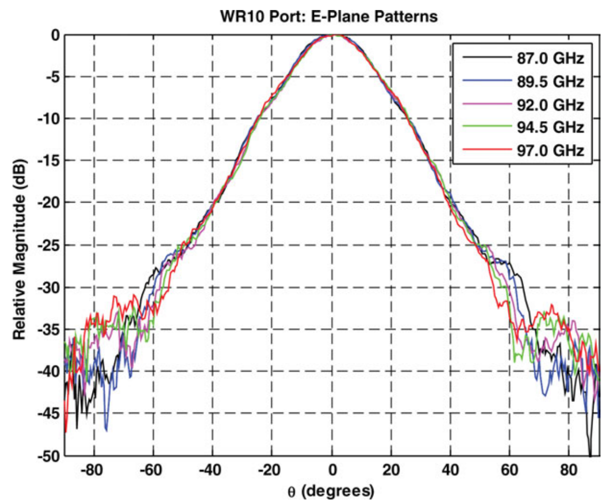

Figure 6 WR10 port measured E plane patterns. [Color figure can be viewed in the online issue, which is available at wileyonlinelibrary.com]

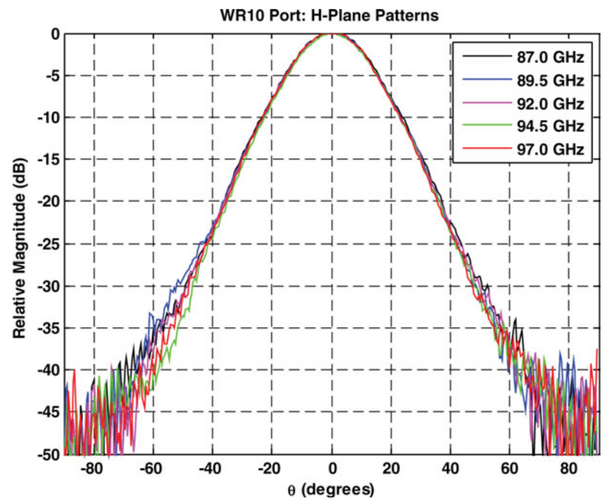

Figure 7 WR10 port measured H plane patterns. [Color figure can be viewed in the online issue, which is available at wileyonlinelibrary.com]

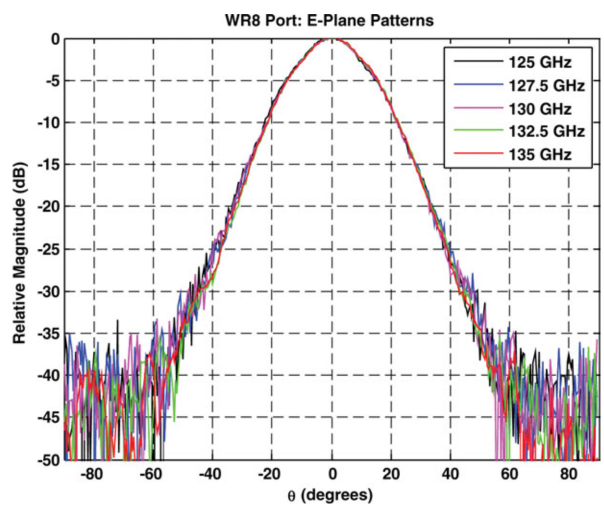

Figure 8 WR8 port measured E plane patterns. [Color figure can be viewed in the online issue, which is available at wileyonlinelibrary.com]

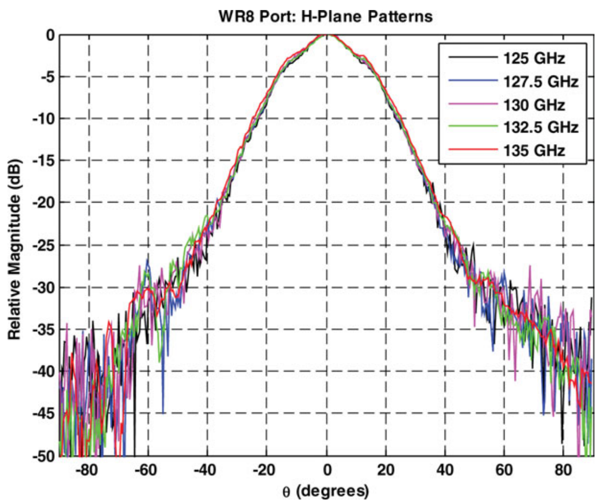

Figure 9 WR8 port measured H plane patterns. [Color figure can be viewed in the online issue, which is available at wileyonlinelibrary.com]

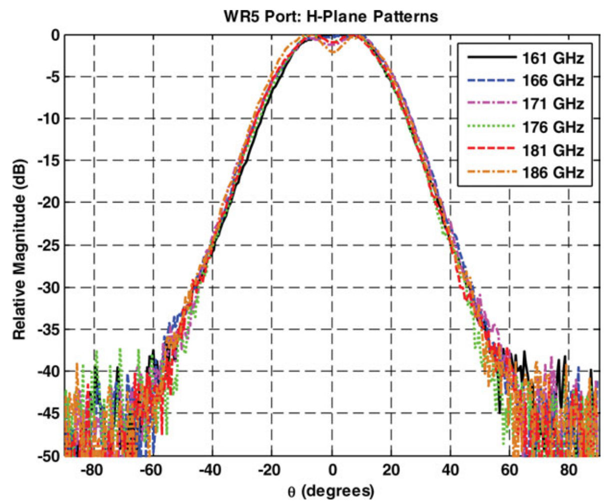

Figure 11 WR5 port measured H plane patterns. [Color figure can be viewed in the online issue, which is available at wileyonlinelibrary.com]

again, even in this band where fabrication errors less than 0.001 inches are quite significant.

Figures 6–11 depict measured E and H plane patterns across all three bands. Pattern measurements were taken on a custom compact range at JPL. As expected, the best fit phase center location was found to be very near the apex of the feed's extended cone, and this common rotation point was used for all pattern measurements in all bands. In addition to the pattern measurements a transmission measurement from the three-frequency feed to a reference feed were made across each band. The purpose of this measurement was to search for narrow band resonances or drop-outs over the entire bandwidth of each port. No such resonances or drop-outs were observed in any band.

Figures 6 and 7 show measured E and H plane patterns for WR10 port excitation between 87 and 97 GHz. Excellent pattern stability in both planes across the band is evident. The edge taper goal of −20 dB at 40 degrees is met very closely in both planes.

Figures 8 and 9 show similar results for the WR8 port and 125–135 GHz band. Here the measured edge taper at 40 degrees ranges from 22 to 25 dB. Excellent pattern symmetry extends across the band.

Patterns in the highest frequency band, 161–186 GHz, are given in Figures 10 and 11. In this band, we observe a slightly different pattern shape than in the lower bands. The flat-top pattern is typical of a flare-angle limited horn operating at the upper edge of its band. This flattened pattern has no significant impact on the overall performance of the reflector-feed system. As we will see below this behavior is predicted by the models. As before the required edge taper is met fairly closely across this 25 GHz band and the measured pattern remains stable as well.

The final three figures show computed and measured E and H plane patterns near the center of each of the frequency bands. The agreement depicted here is typical across all of the frequency bands. The agreement between measured and predicted results is good for all three sample frequencies. Figure 12 shows excellent agreement between predictions and measurements at 92 GHz. Some difference between the measured and computed E plane pattern near the peak is visible in the 130 GHz pattern

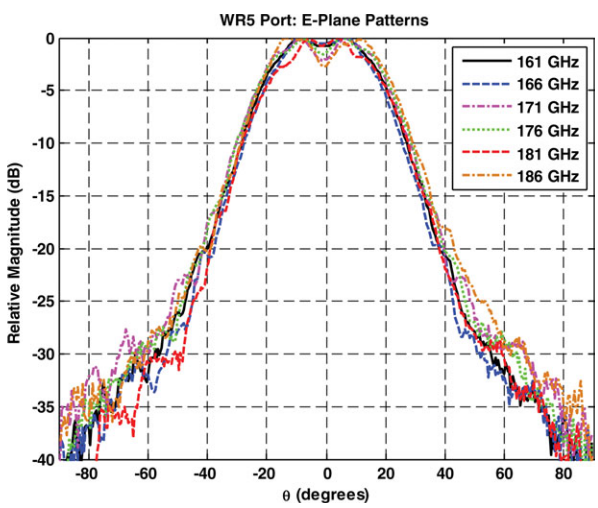

Figure 10 WR5 port measured E plane patterns. [Color figure can be viewed in the online issue, which is available at wileyonlinelibrary.com]

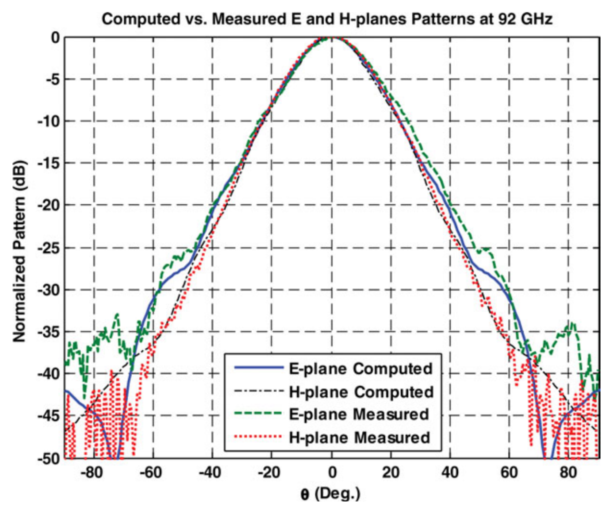

Figure 12 92 GHz measured and computed patterns. [Color figure can be viewed in the online issue, which is available at wileyonlinelibrary.com]

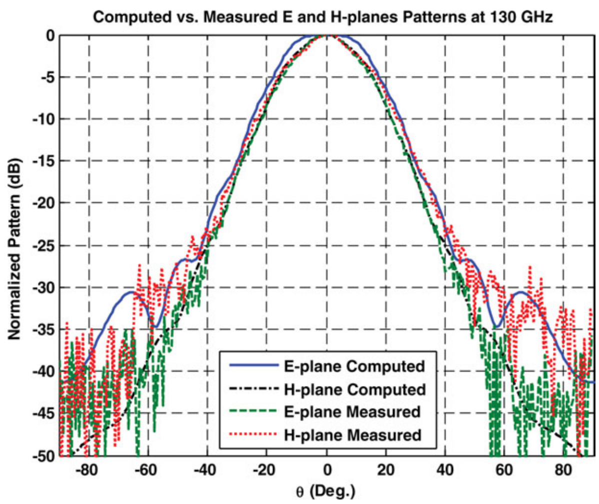

Figure 13 130 GHz measured and computed patterns. [Color figure can be viewed in the online issue, which is available at wileyonlinelibrary.com]

of Figure 13 with general agreement elsewhere, particularly at the edge taper angle of 40°. Figure 14 demonstrates that the measured dip in the center of the pattern in the highest frequency band is in agreement with predictions as well. As expected, the agreement generally degrades slightly with frequency due to tolerance effects compounded by multimode operation of some portions of the feed structure in the WR5 band.

4. CONCLUSION

Results for a three-frequency feed for millimeter-wave radiometry have been presented. Excellent pattern symmetry and return loss have been demonstrated over 10 GHz bands covering 87–97 GHz and 125–135 GHz, as well as a 25 GHz band covering 161–186 GHz. The mechanical aspects of the feed as well as the fabrication techniques used have also been described. The next steps for this project include integration with the three radiometers and demonstration of the complete remote sensing system.

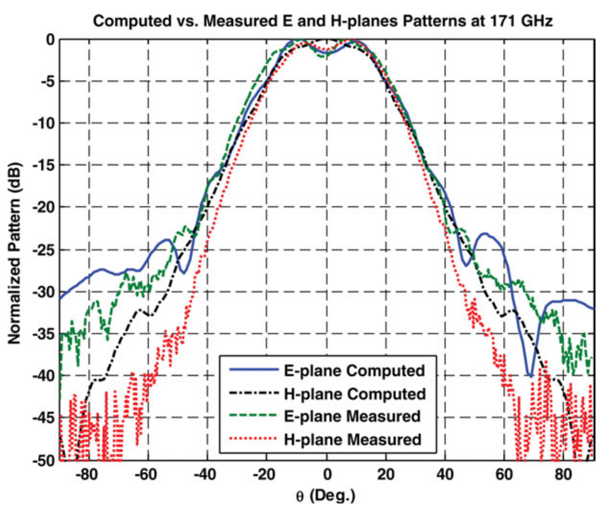

Figure 14 171 GHz measured and computed patterns. [Color figure can be viewed in the online issue, which is available at wileyonlinelibrary.com]

ACKNOWLEDGMENTS

This work was supported by the NASA Earth Science Technology Advanced Component Technology ACT-08 Program. The research described in this article was carried out at the Jet Propulsion Laboratory, California Institute of Technology, and at Colorado State University, under a contract with the National Aeronautics and Space Administration.

REFERENCES

1. M. Durand, L.-L. Fu, D.P. Lettenmaier, D.E. Alsdorf, E. Rodriguez, and D. Esteban-Fernandez, The surface water and ocean topography mission: Observing terrestrial surface water and oceanic submesoscale eddies, Proc IEEE 98 (2010), 766–779.
2. NASA, 2010 Science Plan for NASA's Science Mission Directorate, available at http://science.nasa.gov/media/medialibrary/2010/08/30/2010SciencePlan_TAGGED.pdf. Accessed on November 3, 2011.
3. S.C. Reising, S.T. Brown, P. Kangaslahti, D.E. Dawson, T.C. Gaier, O. Montes, D.J. Hoppe, B. Khayatian, A. Lee, and D. Albers, Advanced component development to enable low-mass, low-power high-frequency microwave radiometers for coastal wet-tropospheric correction on SWOT, In: Proceedings of the NASA Earth Science Technology Forum 2010 (ESTF-2010), Arlington, Virginia, June 2010.
4. W.A. Imbriale, Spaceborne antennas for planetary exploration, Wiley, Hoboken, NJ, 2006. Available at http://descanso.jpl.nasa.gov/Monograph/series8/Descanso8_00_title.pdf.
5. HFSS, ANSYS. Available at http://www.ansoft.com/products/hf/hfss/. Accessed on November 3, 2011.
6. G.L. James and B.M. Thomas, TE11 to HE11 cylindrical waveguide mode converters using ring-loaded slots, IEEE Trans Microwave Theory Tech 30 (1982), 278–285.
7. H. Deguchi, T. Kobayashi, and M. Tsuji, Compact low cross-polarization multimode horn with ring-loaded coaxial grooves, In: IEEE Antennas Propag Soc Int Symp (APSURSI), 2010 IEEE, July 11–17, 2010, pp. 1–4.
8. WASPNET, Microwave Innovation Group (MIG). Available at http://www.mig-germany.com/. Accessed on November 3, 2011.

A MULTISTANDARD DUAL-MODE FULLY-INTEGRATED MINIATURE, LOW-POWER-CONSUMPTION 860–960 MHz CMOS RFID READER FOR MOBILE COMMUNICATIONS, SENSING, AND NETWORKING

Sanghun Lee,[1] Hyukje Kwon,[2] Changho Ryu,[2] Sungwan Kim,[2] Kyoungyong Kang,[2] Seonghun Chun,[2] Pyunghan Lee,[2] and Cam Nguyen[1]
[1] Department of Electrical and Computer Engineering, Texas A&M University, College Station, TX 77843-3128; Corresponding author: platune@tamu.edu
[2] 3A Logics, Seoul, Korea

Received 20 February 2012

ABSTRACT: *A fully-integrated single-chip radio frequency identification (RFID) reader consisting of zero-IF receiver, direct up-conversion transmitter, sigma-delta phase-locked loop synthesizer, and modulation/demodulation (MODEM) module has been developed using 0.18 μm CMOS process. The RFID reader operates from 860–960 MHz in steps of 100/200 kHz, supporting a multiband global standard suitable for USA, Europe, and Korea for both passive and active communication. It is specifically designed to achieve small size, low spur levels, low power consumption, and complete integration while meeting requirements for short-range applications. The developed*